International Journal of Fracture 35: 103–124 (1987)
© Martinus Nijhoff Publishers, Dordrecht – Printed in the Netherlands

Tests and interpretation of mixed mode I and II fully plastic fracture from simulated weld defects

G.A. KARDOMATEAS* and F.A. McCLINTOCK
Massachusetts Institute of Technology, Cambridge, MA 02139, USA
(** present address: General Motors Research Laboratories, Engineering Mechanics Department, Warren, MI 48090-9055, USA*)

Received 23 February; accepted 8 June 1987

Abstract. Most fracture tests use symmetric specimens, with the crack advancing into the relatively undamaged region between two plastic shear zones. A crack near a weld or shoulder, loaded into the plastic range, may have only a single shear band, along which the crack grows into prestrained and damaged material with less ductility than the usual symmetrical configurations. Tests on six alloys show that the crack growth ductility, defined as the minimum displacement per unit ligament reduction, is less in the asymmetric case than in the symmetric one by a factor of 3 for low-hardening alloys (with strain hardening exponents $n \simeq 0.1$). This means that with low-hardening (typically high strength) alloys, the surrounding structure must be 3 times stiffer for fracture-stable design. For higher hardening alloys ($n \simeq 0.23$) the crack growth ductility is less in the asymmetric case by a factor of at most 1.2. The crack initiation ductility (here approximately the crack tip displacement CTD) is relatively unaffected by asymmetry, but it cannot always be relied on for ductility (e.g., in low cycle fatigue). Therefore tests such as these on crack growth ductility are needed for help in design and maintenance of structures.

Triaxiality on one side of the asymmetric shear crack diverts it from 45 deg to 38–41 deg (from the transverse direction), the smaller diversion with less strain hardening. In addition, the far field displacement vector is 51 to 63 deg from transverse, more with high hardening, suggesting a mode I component even where the non-hardening slip line field predicts a pure shear displacement.

1. Introduction

For fracture-stable structures it is important not only that fully plastic conditions be attained before fracture, but also that the load does not fall off too rapidly during crack growth. Flow fields such as the second of Fig. 1, in which the far-field deformation consists of a single shear band, may arise in practice due to the constraint of weld material. These specimens may exhibit less ductility than the symmetric ones, because the crack is advancing into pre-strained and damaged material, rather than into the new material encountered by a crack advancing between two symmetrical shear bands.

Observations show that ductile fracture in an uncracked part results from a three-step process: 1) the cracking of inclusions or the separation of inclusion-metal interfaces; 2) hole growth to localization or coalescence into a crack; 3) crack growth by a similar mechanism, either on a plane of high shear stress, giving elongated dimples, or on a plane normal to the direction of maximum tensile stress, giving equiaxed dimples [1–2].

Ductile or fully plastic fracture in a pre-cracked part consists of an initiation stage, characterized by a crack tip opening displacement (CTOD), and a growth stage which, if stable, may be characterized by a crack tip opening displacement per unit crack growth d(CTOD)/da [3–5]. For small angles, d(CTOD)/da is the crack opening angle, COA. Initiation has been described by the path independent stress-displacement integral J, to which CTOD is

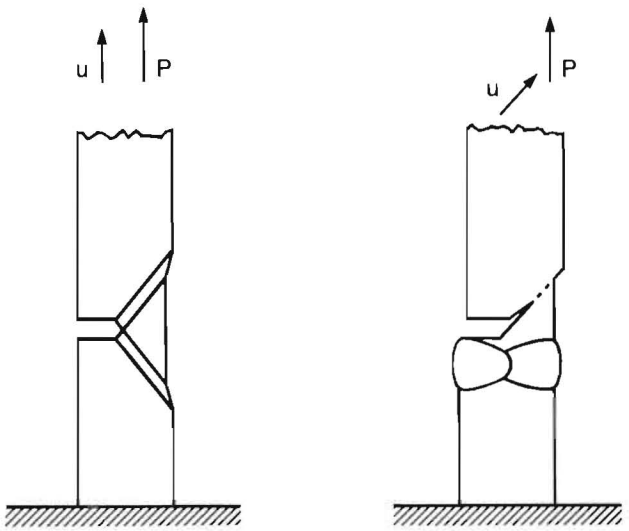

Fig. 1. Ideally plastic deformation of symmetric and asymmetric crack configurations.

proportional. Crack growth is described by the tearing modulus $T = dJ/da$ [6], which is also approximately the crack opening angle COA divided by the elastic strain at the tensile strength, T.S./E (these relations will both be derived below in Section 2c, Interpretation of tests).

In general, ductile fracture occurs by hole growth, which depends on the combined history of stress, strain, and rotation near the crack tip, where the holes are growing. The validity of a single measure for fracture, such as CTOD or J, depends on the presence of a stress-strain singularity near the crack tip that is governed by a single scalar quantity. For initiation the HRR [7–8] singularity indeed often dominates as shown by finite element studies [9]. Singular fields for growth seem to be available only for the elastic-plastic case [10–14]. Because of a finite fracture process zone size, they probably do not dominate when strains are large compared to the elastic strain all across a section, from the hole growth in the fracture process zone to the far boundary. Nonetheless, data are often presented as if a single dominant singularity existed, or perhaps in the hope that it does. For instance, typical values of d(CTOD)/da for various bend tests are given in Table 1. In the limit of no strain hardening, it is well known that a variety of stress and strain states exist at the crack tip, depending on the geometry and mode of loading [16]. Reduced ductility has been shown in a configuration giving a high strain concentration, even at the expense of reduced triaxiality [17].

The fractography of pure mode II loading was studied by Jones and Chisholm [18]. The ductility in pure mode II loading was measured by Chant et al. [19] on high hardening carbon manganese steel (B.S. 1501-151-430A, Y.S. = 329 MN/m^2, T.S. = 490 MN/m^2). They found the ductility, measured by dJ/da, to be practically the same in mode II and mode I, although the microscopic features were different for the two modes.

The tests described here deal with the possibility of unexpectedly low ductility, as is found in practice for asymmetric crack configurations in plates near welds or shoulders (Fig. 1). Here there is *mode II deformation under combined mode I and II loading*. As Paris et al. [6] have shown, low crack growth ductility can lead to instability of structures.

Table 1. Typical values of crack tip opening displacement per unit crack growth for symmetrical tests. All fatigue-precracked

Material	Test, thickness	d(CTOD)/da ≃ COA, radians	Ref.
A533B steel Y.S. = 443 MN/m² T.S. = 574 MN/m²	Compact tension 102 mm th. 93°C	0.205	[3], [15]
ASTM A471 rotor steel Y.S. = 931 MN/m² T.S. = 1022 MN/m²	3-point bend 203 × 25 × 13 mm a/w = 0.502**	0.164*	[6]
Free cutting mild steel, annealed	3-point bend 5–17 mm th.	0.300	[5]
BS 4360 Grade 50 steel Y.S. = 359 MN/m² T.S. = 526 MN/m²	3-point bend 25 mm th.	0.250	[4]

* Taken to be tearing modulus times elastic strain at tensile strength, T × (T.S./E).
** a = crack length, w = specimen width.

Near the tip of a crack growing in a single shear band, strain hardening causes the deformation field to fan out. For power law creep or deformation theory plasticity, the stress and strain in the neighborhood of a stationary crack can be found from Shih's mixed mode solutions [20]. For a growing crack, a fully-plastic, incremental plasticity solution should be obtained, taking into account the hardening of the material left behind the growing crack. Pending such an analysis, McClintock and Slocum [21] used a superposition of strain increments adapted from Shih's analysis. The crack was assumed to follow the center of the 45 deg shear band. The axial displacement for initiation, u_i, with a band at ϕ from the transverse direction, was given in terms of the flow stress at unit strain $\bar{\sigma}_1$, the shear yield strength k, the mean inclusion spacing ϱ, the critical fracture strain γ_c, and the strain hardening exponent n:

$$u_i = \frac{\bar{\sigma}_1}{k} I_{1/n} \varrho \left(\frac{\gamma_c}{2\tilde{\varepsilon}}\right)^{n+1} \sin \phi, \tag{1}$$

For the assumed pure mode II deformation, $\tilde{\varepsilon} = 0.88$ [20]. For $n = 0.1$–0.2, $I_{1/n} = 0.72$–0.83. For $\bar{\sigma}_1/k = 3$ and $\gamma_c = 0.8$, the initiation displacement was of the order of the inclusion spacing ($\varrho \simeq 0.01$ mm). For a quasi-steady growth, the crack advance per unit displacement was practically insensitive to the strain hardening exponent n:

$$\frac{d(u/u_i)}{d(c/\varrho)} = \frac{n+1}{\ln\left[(c - c_i)/\varrho + \exp(n+1)\right]}. \tag{2}$$

The above formula, for a mean inclusion spacing $\varrho = 0.01$ mm and crack growth over the ligament length of $l_0 = 2.54$ mm, gives $du/dc \simeq 0.2$. These results will be discussed and compared with the experimental findings below in Section 3c. To correct for triaxial effects

around the crack tip, we considered several sites around the current crack tip [22]. The damage at each site due to the deformation for crack initiation and prior growth was determined and then the crack was grown in the direction requiring the least increment in far field displacement. While the results were generally as expected, some numerical inconsistencies have appeared, so the results unfortunately cannot be relied on.

The objective here is a detailed experimental study and interpretation, for several alloys, of crack configurations such as shown in Fig. 1b, that grow along a single shear band under combined shear and tensile loads.

2. Experimental procedures

(a) Material

Tensile tests were performed on six alloys with the compositions and conditions listed in Table 1, using standard 6.35 mm diameter specimens with 25.4 mm gauge length. Curves of true stress $\bar{\sigma}$ vs. integrated equivalent plastic strain $\bar{\varepsilon}^p$ are represented by

$$\bar{\sigma} = \bar{\sigma}_1(\varepsilon_0 + \bar{\varepsilon}^p)^n. \tag{3}$$

The Bridgman correction for necking was applied with the ratio of net section radius a to profile radius R found from the empirical relation that it increases directly with the amount that the strain exceeds the uniform strain [23]: $a/R = \varepsilon - \varepsilon_u$.

The three constants $\bar{\sigma}_1$, ε_0, and n were fitted three ways: i) to the yield strength YS, the tensile strength TS and the load maximum there, and the logarithmic (uniform) strain at the tensile strength ε_u; ii) to the tensile strength conditions and the equivalent true strength and strain at fracture σ_f and ε_f; and iii) to the YS and the flow strengths taken rather arbitrarily at $\bar{\varepsilon}^p = 0.125$ and $\bar{\varepsilon}^p = 0.250$. The results fell in the ranges shown in Table 2. We denote as "lower hardening alloys" the 1018 cold finished, the HY-80, and the HY-100 steels ($n \simeq 0.1$); and as "higher hardening alloys" the 1018 normalized and A36 hot rolled steels ($n \simeq 0.2$). The 5086-Hill aluminium is between these two groups.

(b) Test method

Both the symmetric and asymmetric notched specimens were first fatigue precracked and then tested in tension. Specifically, from 12.7 mm diameter round bars of each alloy, seven specimens were first machined as shown in Fig. 2a, with side grooves to ensure a straight fatigue pre-crack approximately 1.3 mm deep with a root radius of 0.25 mm. After fatigue pre-cracking, the asymmetry in the four asymmetric specimens was introduced through the machined shoulder (Fig. 2b). In addition, the further side grooves were machined at 40 deg from the transverse direction. This corresponded to the crack direction found in preliminary tests and helped to maintain plane strain conditions and to give planar cracks with straight fronts. For the three symmetric specimens, since the crack grows by alternating shear at ± 45 deg, orthogonal triangles were machined as shown in Fig. 2c.

Stability of the tests turned out to be an important consideration due to the high crack growth rate expected in the asymmetric case. Thus short specimens, stiff adapters, and

Table 2. Room temperature tensile and hardness data for the six alloys tested

Yield		Tensile		Hardness	Fracture			Parameters in Eqn. (3)		
Strength	Strain	Strength	Unif.strn		RA	True		Strength	Prestrain	Exponent
						Strg	Strn			
Y.S.,	ε_y	T.S.,	ε_u	HDP		σ_f,	ε_f	σ_1	ε_0	n
MPa,	–	MPa,	–	Kgf/mm^2	%	MPa,	–	MPa	–	–
1018 steel (0.15–0.20% C, 0.60–0.90% Mn) cold finished										
411	0.002	500	0.04–0.086	180	52	660	0.72	590–690	–0.02–0.01	0.04–0.13
HY-80 steel (0.18% C, 2–3.25% Ni, 0.10–0.40% Mn, 0.15–0.35% Si)										
648	0.002	745	0.13	209	71	1200	1.25	1030–1150	0.007–0.043	0.10–0.17
HY-100 steel (0.20% C, 2.25–3.50% Ni, 0.10–0.40% Mn, 0.15–0.35% Si)										
772	0.002	869	0.072	248	71	1350	1.24	1100–1280	0.001–0.111	0.06–0.18
5086–H111 aluminum (4% Mg, 0.4% Mn, 0.15% Cr)										
225	0.002	333	0.15	82	44	480	0.58	510–540	0.002–0.010	0.15–0.18
1018 steel, normalized 1700°F in argon										
351 UYP										
305	0.028	457	0.17	103	70	830	1.19	690–770	–0.025–0.100	0.14–0.27
A36 steel (0.29% max C, 0.60–0.90% Mn) hot rolled										
411 UYP										
337	0.032	469	0.24	90	68	880	1.14	800–840	–0.020–0.022	0.20–0.26

locknuts were used. The tensile tests were performed on a 0.5 MN (50 metric ton) MTS testing machine with compliances of 2.3×10^{-6}, 4.6×10^{-6}, 1.08×10^{-6} mm/N for the steel specimens, the adapters (including a pin-joint), and the machine, respectively. Freedom of transverse displacements was ensured by attaching the upper end of the specimens to a U-joint. Stable tests were obtained except for the lower hardening alloys, which were dynamic for less than 20 percent of the falling part of the load-displacement curve.

The load was plotted continuously versus the axial displacement across the shoulders, as measured with a strain gauge extensometer. In addition, a strain gauge transverse displacement meter gave relative displacements between extension arms so that the measurement was made at the net section, as shown in Fig. 3.

(c) Interpretation of tests

A typical plot of load vs. axial displacement is shown in Fig. 4. It can be idealized as a trapezoid consisting of an initial line corresponding to the elastic compliance across the 25-mm gauge length, a horizontal line at the maximum load, and a line tangent to the steepest part of the falling curve, associated with crack growth. The displacement corresponding to the horizontal line is called the *idealized crack initiation displacement*, u_i^I. Since for a rigid-plastic material in this configuration the relative far-field displacement is the same as the crack tip displacement, the idealized initiation displacement is an approximation to

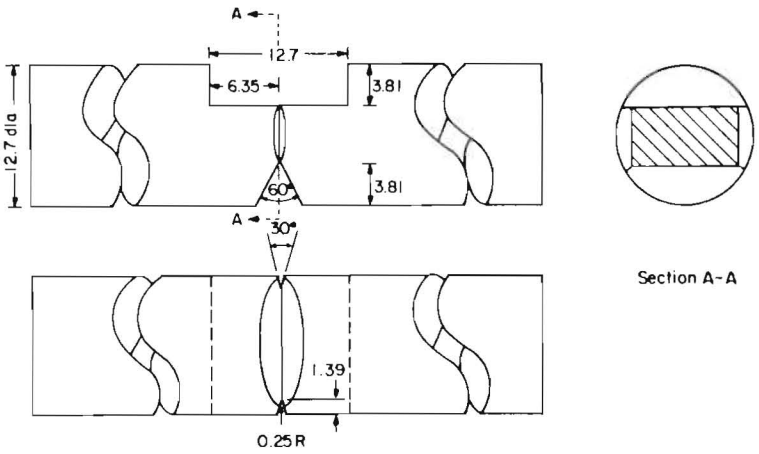

Fig. 2a. Machining for precracking of the specimens.

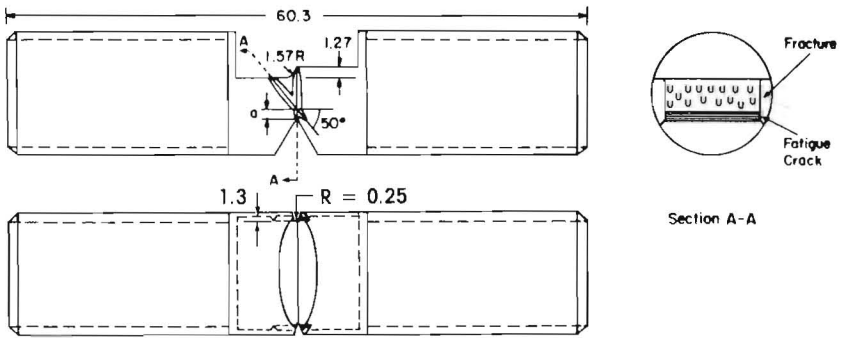

Fig. 2b. Second machining (after fatigue precracking) for the asymmetric specimens; a is the fatigue crack.

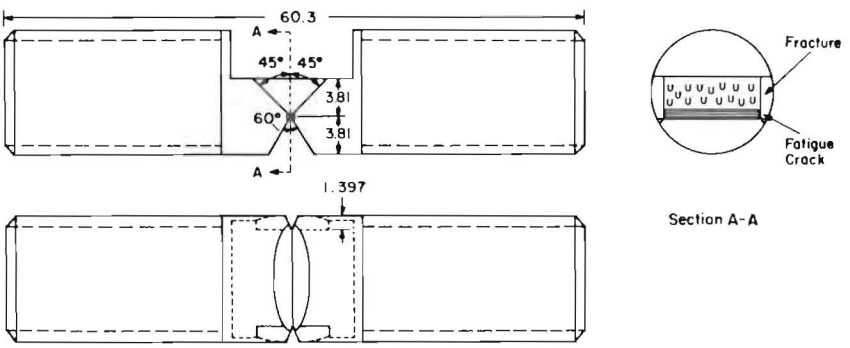

Fig. 2c. Second machining (after fatigue precracking) for the symmetric specimens.

the crack tip displacement. Although the plots like Fig. 4 were normalized by dividing by the gauge length, the crack tip displacements for initiation are local quantities and should be independent of specimen size, so they will be given in terms of physical length. They are also then easier to compare with the more familiar crack tip opening displacements (CTOD) for mode I.

The maximum load is normalized as the *load factor*, defined as the ratio of maximum load to a nominal load which is the limit load for a non-hardening material with the same tensile

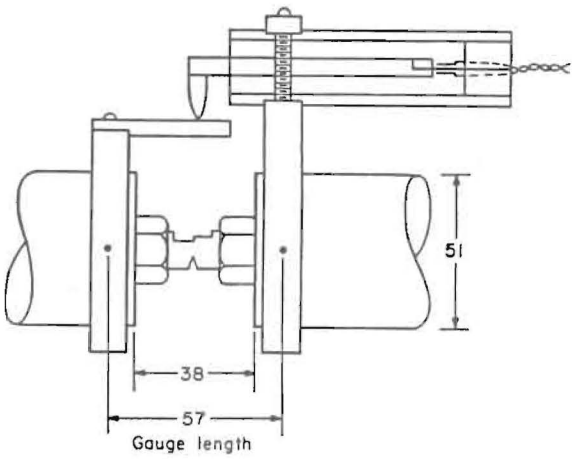

Fig. 3. Axial and transverse displacement gauge locations.

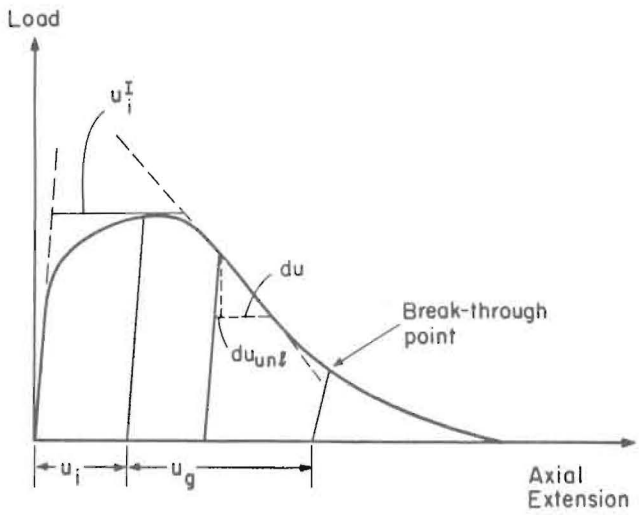

Fig. 4. Schematic of the load vs. axial gauge-point displacement curve. The displacements u_g and u_i are measured after fracture. The crack growth displacements is $du_c = du + du_{unl}$.

strength. For the single-edge-notch specimens tested here, the nominal load is given in terms of the initial projected ligament length l_0 after pre-cracking, the width w, and the tensile strength T.S. by

$$P_{\text{nom}} = l_0 w(\text{T.S.})(2/\sqrt{3}). \tag{4}$$

Then the *load factor* F_L is

$$F_L = P_{\max}/P_{\text{nom}}. \tag{5}$$

The most useful measure of crack growth resistance seems to be the *crack growth ductility*, D_g, defined as the minimum axial displacement per unit projected ligament reduction.

Thinning of the ligament from the far side in fully plastic flow makes the reduction in ligament, rather than the crack advance, more appropriate for describing load drop. To reduce the effects of compliance, the *crack growth displacement* du_g is taken to consist of the gauge displacement du and the elastic unloading du_{unl} as shown in Fig. 4.

$$du_g = du + du_{unl}. \tag{6}$$

The ligament reduction can be approximated from the relative load drop, and thus we define:

$$D_g \equiv \left(\frac{du_g/l_0}{dP/P_{max}}\right)_{min} \simeq \left(\frac{du_g}{dl}\right)_{min}. \tag{7}$$

From Fig. 5, using the law of sines gives the relation of D_g to the crack opening angle:

$$D_g = \frac{u_g}{l_l} = \frac{\sin\phi \sin(\mathrm{COA})}{\cos\theta_l \sin(\phi - \theta_l + \mathrm{COA})}. \tag{8}$$

In addition, the crack growth ductility is the normalized compliance requirement for fracture-stable design:

$$\text{Compliance of surroundings} < D_g l_0/P_{max}. \tag{9}$$

If it is not convenient to measure the cracked compliance giving du_{unl}, an *extensometer ductility* D_{ext} is defined as

$$D_{ext} \equiv \left(\frac{du/l_0}{dP/P_{max}}\right)_{min} \simeq \left(\frac{du}{dl}\right)_{min}. \tag{10}$$

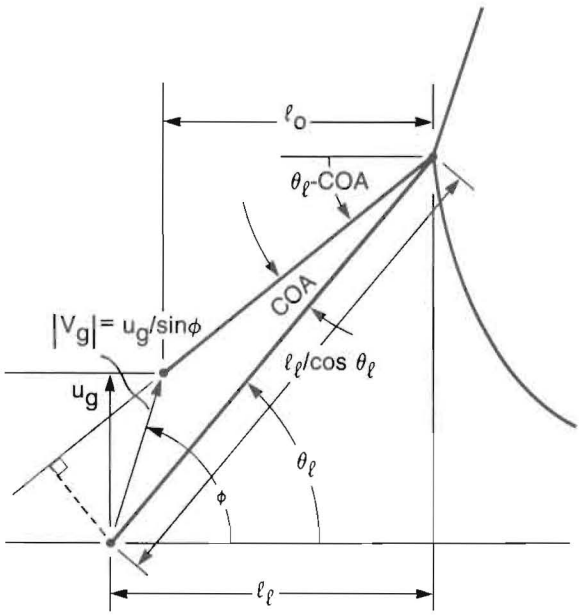

Fig. 5. Deriving the relation between the crack opening angle and the crack growth rate.

This definition includes the effect of the compliance in the shoulders and is thus smaller than D_g.

The crack growth ductility gives a parameter analogous to the tearing modulus of Paris et al. [6] defined in terms of the yield or tensile strength σ_0, the modulus E and the J-integral by:

$$T = \frac{E}{\sigma_0^2}\frac{dJ}{dc}. \tag{11}$$

To approximate the J-integral, consider the simple case of the far-field displacement taking place along a single shear band and express it in terms of the shear strength, k, and the displacement across the band, $u\sqrt{2}$, which breaks through to the back surface where the band is of thickness t. The J integral in terms of work per unit volume W and traction T is

$$J = \int\left(W dx_2 - T_j\frac{\partial u_j}{\partial x_1}\,ds\right). \tag{12}$$

The only nonzero term occurs where the shear band breaks through the back surface along a distance $\Delta x_2 = t\sqrt{2}$, where $W = ku\sqrt{2}$:

$$J = (ku\sqrt{2})(t\sqrt{2}) = 2ku. \tag{13}$$

Thus define a *modified tearing modulus* T^*, analogous to the tearing modulus T, by introducing (13) into (11). In terms of the tensile strength, $\sigma_0 \simeq T.S. \simeq k\sqrt{3}$,

$$T^*_{\text{asym}} = \frac{E}{(T.S.)^2}\,2k\frac{du}{dc} \simeq \frac{E}{T.S.}\frac{2}{\sqrt{3}}D_g. \tag{14}$$

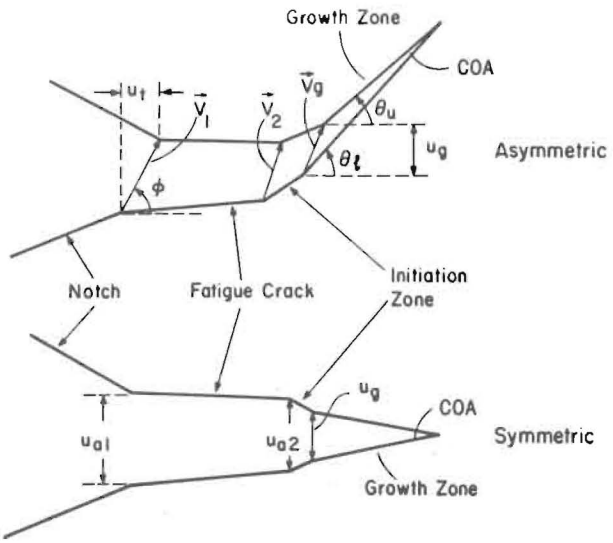

Fig. 6. Schematic of the fracture surface profile for the asymmetric and symmetric cases.

In the symmetric case the expression for the J-integral, $J_{sym} = 2ku$ [16], leads to an identical expression.

More accurate measurements of the displacements during crack initiation and growth, u_i and u_g, are found from the profiles of the two crack surfaces, plotted using a metallurgical microscope with a travelling stage. Numerous horizontal and vertical coordinates were recorded through two linear potentiometers driving an x-y recorder. A typical plot, as in Fig. 6, consists of the 60 deg notch, the fatigue crack (with some amount of deformation, $\boldsymbol{v}_1 - \boldsymbol{v}_2$), an initiation zone which shows some blunting, and a growth zone. The initiation displacement is $\boldsymbol{v}_1 - \boldsymbol{v}_g$. In addition, fracture profiles were used to obtain the crack opening angle COA, the lower and upper flank angles θ_l and θ_u, the average crack direction $\theta_c = (\theta_u + \theta_l)/2$, and, for the asymmetric case, the orientation of the total displacement vector ϕ. The breakthrough displacement, when the fracture first breaks through the back surface and leaves shear lips at the sides, is given by the vertical component of $\boldsymbol{v}_1$, and is usually indicated by a flattening of the load-extension curve.

3. Results

Plots of load and transverse displacement versus axial displacement are shown in Figs. 7 and 8 for symmetric and asymmetric specimens of HY-100 and A36 HR steels, typical of low and high hardening alloys. The predominant features for these and the other alloys are summarized in Table 3, along with data obtained from the fracture profiles, such as shown in Figs. 9 and 10.

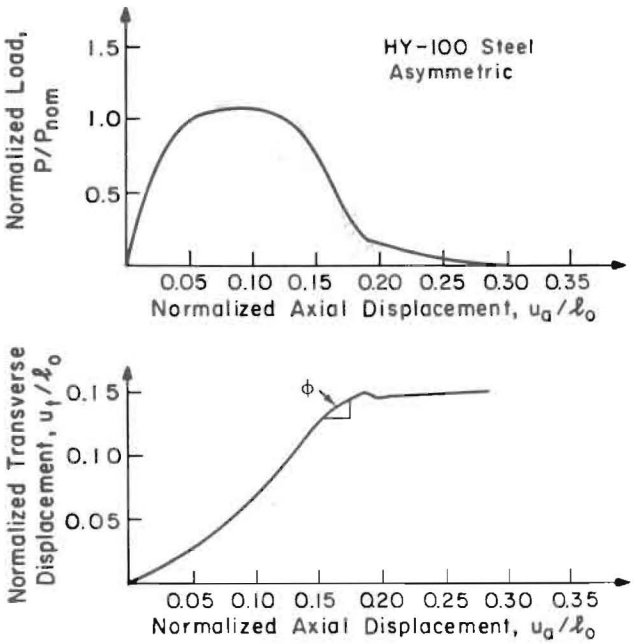

Fig. 7a. Test data for the HY-100 steel asymmetric specimens.

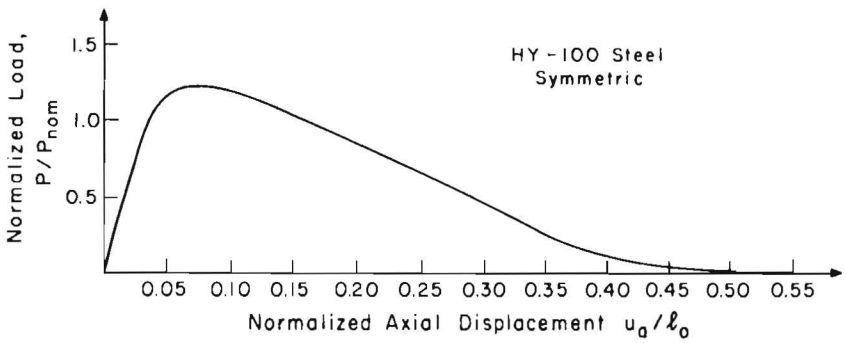

Fig. 7b. Test data for the HY-100 steel symmetric specimens.

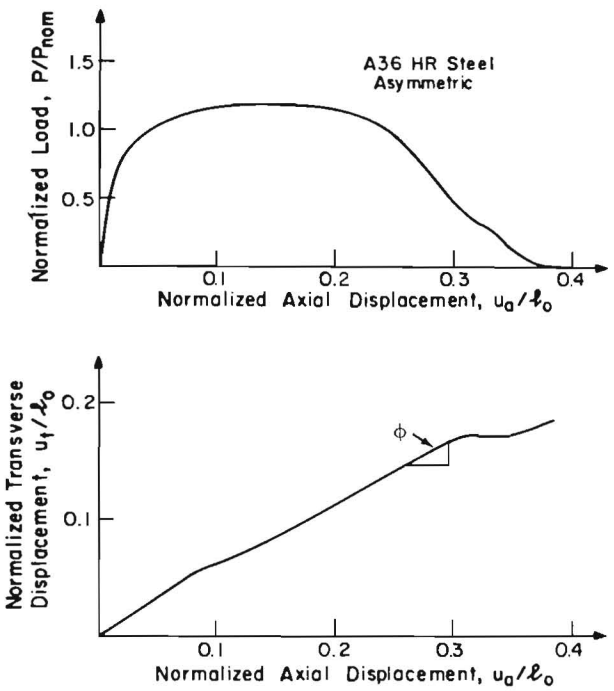

Fig. 8a. Test data for the A36 hot rolled steel asymmetric specimens.

Before considering the results in detail, note the major results. For the low-hardening HY-100 steel, the falling part of the load-displacement curve for the asymmetric specimens (Fig. 7a) is much steeper than that of the symmetric specimens (Fig. 7b). Thus the asymmetric specimens of HY-100 require a much stiffer surrounding structure for stability. For the high hardening A36 HR steel, the load-deformation curves for the asymmetric specimens fall off only a little more steeply (Figs. 8a vs. 8b). This corresponds to the large decrease in the crack opening angle of the asymmetric vs. the symmetric specimens of the low-hardening HY-100 steel (Figs. 9a, 9b), compared to the negligible increase for the high hardening A36 steel (Figs. 10a, 10b). The reader interested primarily in these major results may wish to turn directly to d) Crack growth ductility measures.

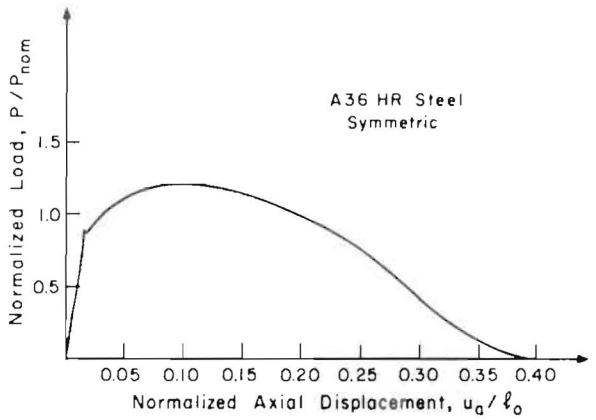

Fig. 8b. Test data for the A36 hot rolled steel symmetric specimens.

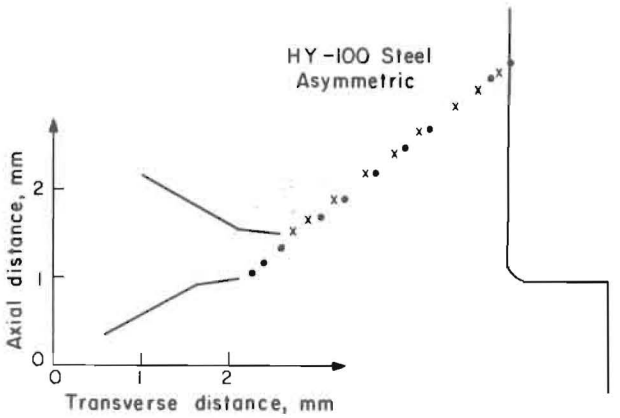

Fig. 9a. Fracture surface profile for the HY-100 steel asymmetric specimens.

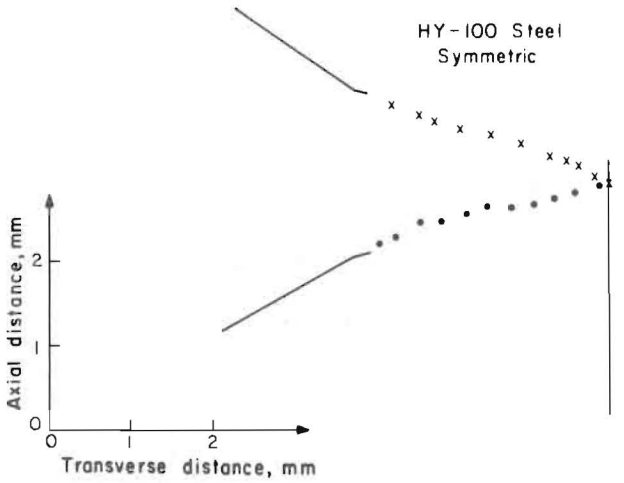

Fig. 9b. Fracture surface profile for the HY-100 steel symmetric specimens.

Table 3. Test results

	Averages of 3 symmetric and 4 asymmetric tests. (Ligament $l_0 = 2.5$ mm)					
Alloy	1018 CF	HY-80	HY-100	5086-H111	1018 Norm.	A36 HR
n =	0.12	0.13	0.12	0.16	0.20	0.23
a) *Initiation ductility measures*						
Idealized initiation displacement, u_i^I, mm (Fig. 4)						
Sym	0.183	0.274	0.211	0.455	0.854	0.437
Asym	0.185	0.279	0.254	0.409	0.640	0.523
Profile initiation displacement, u_i, mm (Fig. 6)						
Sym	0.053	0.130	0.130	0.201	0.544	0.203
Asym	0.084	0.183	0.132	0.185	0.386	0.279
b) *Maximum load*						
Load factor, $F_L = P_{max}/l_0 w(T.S.)(2/\sqrt{3})$ (Eqn. 4)						
Sym	1.02	1.16	1.15	1.19	1.29	1.21
Asym	0.88	1.05	1.06	1.12	1.15	1.20
c) *Directions: far-field displacement and crack growth*						
Relative far-field displacement direction, ϕ (Fig. 6)						
Sym			($\simeq 90°$)			
Asym	51°	55°	55°	56°	63°	61°
Crack direction $\theta_c = (\theta_u + \theta_l)/2$ (Fig. 6)						
Sym			($\simeq 0°$)			
Asym	41°	40°	40°	40°	38°	38°
d) *Crack growth ductility measures*						
Crack growth ductility, $D_g \equiv (du_c/dl_0)/(dP/P_{max})_{min} \simeq (du_c/dl)_{min}$ (Eqn. 7)						
Sym	0.233	0.320	0.354	0.166	0.258	0.192
Asym	0.072	0.096	0.105	0.108	0.215	0.181
Modified tearing modulus, $T^* \equiv (E/T.S.)(2/\sqrt{3})D_g$ (Eqn. 14)						
Sym	90.9	107.9	103.8	43.6	144.3	108.8
Asym	28.2	32.4	47.4	28.4	115.2	102.6
Extension rate, $D_{ext} \simeq (du/dl)_{min}$ (over 25 mm gauge length) (Eqn. 10)						
Sym	0.199	0.285	0.299	0.120	0.237	0.165
Asym	0.046	0.060	0.061	0.083	0.195	0.154
Profile growth displacement, u_g/l_0 (Fig. 6)						
Sym	0.262	0.362	0.404	0.278	0.317	0.254
Asym	0.084	0.115	0.125	0.138	0.230	0.216
Crack opening angle from crack growth ductility, COA (Eqn. 8)						
Sym	13°	18°	20°	9.5°	15°	11°
Asym	0.7°	1.3°	1.5°	1.6°	4.7°	3.7°
Profile crack opening angle, COA $= \theta_l - \theta_u$, (Fig. 6)						
Sym	18°	26°	28°	18°	24°	20°
Asym	1°	2°	2°	2°	6°	5°

(a) Initiation ductility measures

Idealized initiation displacement, u_i^I. As shown in Table 3, this experimentally convenient measure of the crack tip displacement (defined in Section 2c) is not appreciably different for the asymmetric and symmetric configurations. It is, however, dependent on strain hardening: for the higher hardening alloys it is two to four times that for the lower hardening ones.

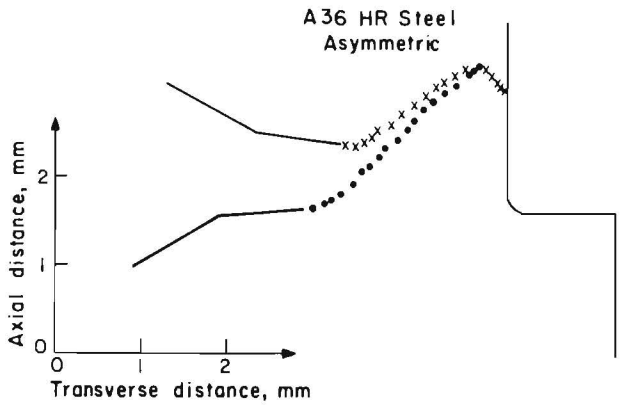

Fig. 10a. Fracture surface profile for the A36 hot rolled steel asymmetric specimens.

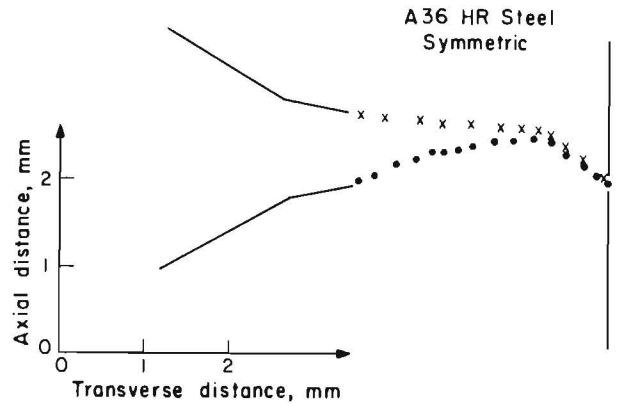

Fig. 10b. Fracture surface profile for the A36 hot rolled steel symmetric specimens.

Profile initiation displacement, u_i. This more accurate initiation displacement, from fracture surface profiles, is given in the next pair of rows of Table 3. It is about 0.5 of the idealized initiation displacement, although ratios as low as 0.3 and as high as 0.7 are found in cold-rolled vs. normalized 1018 steel.

Both experimental observations of initiation displacement are larger by an order of magnitude or more than the 0.01 mm dimple or crack nucleus spacing of (1), found using the Shih mixed mode strain hardening singularities but neglecting blunting. Similar results appear to be found by considering the effects of triaxiality around the crack tip but also neglecting blunting [22]. These results highlight the importance of taking blunting into account in any theoretical calculations of crack initiation [24–25].

(b) Maximum load

In Table 3 the maximum load is characterized by the load factor of [17], which is the maximum load divided by the limit load of nonhardening material based on the tensile strength (4), (5). The load factors are in general somewhat larger in the higher hardening alloys, where there is more strain-hardening around the initial notch, and for the symmetric cases, where more ductility allows higher strain-hardening.

(c) Directions

Far-field displacement vector. In the asymmetric case, the angle ϕ of the far-field displacement vector from the transverse direction, defined from the slope of the transverse vs. axial displacement curves such as Figs. 7a and 8a, is greater than 45 deg and larger in the higher hardening alloys. The final relative far-field displacement vector $\boldsymbol{v}_1$ at ϕ, measured after fracture from the microscopic profile plots (Fig. 6), is between 51 and 63 degs. It is larger for the higher hardening alloys. The fact that it is typically greater than 45 deg means that there is some mode I (opening) component of the crack tip displacement, beyond that associated with cracking to one side of a single 45 deg shear band in non-strainhardening materials.

Crack direction. In the symmetric specimens the macroscopic crack generally ran within 10 deg of transverse. "Zig-zagging" of the fracture surface is characteristic of the 5086-H111 aluminum symmetric specimens, where two slip planes were active and the crack grew by alternating shear. The wavelength increased from 50 to 200 μm as the crack grew. In the end the fracture turned into a shear lip. Symmetric specimens in the lower hardening alloys also often turned into asymmetric ones, following only one slip plane. In some instances, half of the specimen followed the $+45$ deg slip plane and half the -45 deg plane.

In the asymmetric specimens, the crack progressed at an angle of about $\theta_c = 38$–41 deg from the transverse (Table 3). Relative to the shear band as determined from the far-field displacement, the crack was more transverse by $\phi - \theta_c = 10$–25 deg, the more the higher the hardening. This is perhaps because these far-field and local crack tip displacement vectors measured from the surface profiles were in different directions, rather than being parallel. Furthermore, this deviation from the shear band direction is expected from the higher triaxiality to one side of the crack tip displacement vector.

(d) Crack growth ductility measures

Crack growth ductility, D_g. In the low hardening alloys, the asymmetric crack growth ductility, defined in (7), is less than the symmetric one by a factor of more than 3. Thus these alloys have 3 times the stiffness requirements for stability. In the high hardening alloys, on the other hand, D_g is less for the asymmetric geometry by only a factor of 1.2, at most. Expressed another way, in the asymmetric case the crack growth ductility in the lower hardening alloys is about 2 times less than in the higher hardening alloys. In the symmetric case, on the other hand, the crack growth is practically insensitive to strain hardening.

Modified tearing modulus, T^*. The tearing modulus T of Paris et al. [6] is approximated from the crack growth ductility for the asymmetric and the symmetric cases from (14). The asymmetric values are lower than the symmetric ones by a factor of 2 to 3 for the low hardening alloys, compared to factors of only 1 to 1.5 for the high hardening ones.

Extension rate, D_{ext}. If it is inconvenient to obtain the compliance near the steepest fall in the load-displacement curve to find D_g, the extensometer ductility, D_{ext}, defined in (10) may be used. It is lower than the crack growth ductility by 0.02 to 0.05, with some tendency for the larger difference to occur with the larger ductilities. The difference emphasizes the difficulty of fracture-stable design, since the net-section compliance it represents would not normally be included in calculating the compliance of the surrounding structure.

Profile displacement during growth, u_g/l_0. The displacement during growth from initiation until the fracture breaks through the back of the specimen, u_g, can be found from the fracture surface profiles (Fig. 6). Its normalized value, u_g/l_0, is in general only 10 to 20 percent larger than the crack growth ductility (except 25 percent for the aluminum alloy), indicating the validity of both measures.

Crack opening angle, COA. In the HY-100 steel, notice from Fig. 9 the large reduction in the crack opening angle (COA) of the asymmetric case relative to that of the symmetric, whereas in the A36 steel of Fig. 10 the difference in the COA between the two geometries is not appreciable. In Table 3, the COA is estimated from the crack growth ductility using (8), and also is given as found from the fracture profiles. For the asymmetric specimens the estimated COA's are low by a factor of 1.2 to 1.5, whereas for the symmetric specimens they are low by a factor of 1.5 to 2. With one exception the ranking is correct; the disagreement is apparently due to error in reading the angles from the profiles, in view of the excellent agreement between the crack growth ductility D_g and the profile displacements u_g/l_0.

(e) Size effects in fully plastic crack growth

Results of tests on 38.1 mm diameter specimens of 5086-H111 aluminum are compared with those from the 12.7 mm specimens in Table 4. As expected, the crack tip opening displacement at initiation, $u_i = 0.19$ mm, is almost exactly the same for the two sizes. The maximum load was 5 percent higher, for no apparent reason. The crack growth ductility, as indicated by the displacement for growth across the ligament, u_g/l_0, was only 4 percent less for the large specimens.

For the size effects predicted by (2), use the mean inclusion spacing of about 10 microns and find the ratio of the crack growth rate for the large to that for the small specimens:

$$\frac{(dc/du)_{\text{large}}}{(dc/du)_{\text{small}}} = \frac{\ln\,[(c - c_i)/\varrho]_{\text{large}}}{\ln\,[(c - c_i)/\varrho]_{\text{small}}} = \frac{\ln\,(762)}{\ln\,(254)} = 1.20.$$

Thus the integration of stationary crack fields gives a size effect due to an increasing crack advance per unit displacement that is small, but still more than observed in these experiments. Eventually, for large enough parts to give elastic-plastic fracture, there will of course be a size effect.

(f) Marking the crack front

In the large 38.1-mm diameter 5086-H111 aluminum specimens, the crack front was marked by imposing unloading-loading cycles at selected points during crack advance. The spacing of these fatigue marks was measured with a stereo microscope at about 50x. The corresponding displacements were then obtained from the load-displacement curves, accurate to about 0.01 mm. Figures 11a, b show the load-displacement curves and Fig. 12 the crack growth-displacement data. The corresponding crack growth ductility can be calculated from (7) as $\Delta u/(\Delta c + \Delta u)$. For the symmetrical specimens there is an acceleration of crack growth. The average D_g is found to be 0.22, while that from the last two points of Fig. 12 is 0.16, compared to the values for large specimens of 0.165. For the asymmetrical specimens, the crack growth

Table 4. Size effect in 5086-H111 aluminum alloy

Initial ligament, l_0, mm	2.54	7.62
a) *Initiation ductility measures*		
Idealized initiation displacement, u_i', mm (Fig. 4)		
Sym	0.455	0.617
Asym	0.409	0.549
Profile initiation displacement, u_i, mm (Fig. 6)		
Sym	0.201	0.198
Asym	0.185	0.183
b) *Maximum load*		
Load factor, $F_L = P_{max}/l_0 w(T.S.)(2/\sqrt{3})$ (Eqns. 4, 5)		
Sym	1.19	1.21
Asym	1.12	1.18
c) *Directions: far-field displacement and crack growth*		
Relative far-field displacement direction, ϕ (Fig. 6)		
Sym	($\simeq 90°$)	
Asym	56°	57°
Crack direction $\theta_c = (\theta_u + \theta_l)/2$ (Fig. 6)		
Sym	($\simeq 0°$)	
Asym	40°	40°
d) *Crack growth ductility measures*		
Crack growth ductility, $D_g \equiv (du_c/dl_0)/(dP/P_{max})_{min} \simeq (du_c/dl)_{min}$ (Eqn. 7)		
Sym	0.166	0.165
Asym	0.108	0.105
Modified tearing modulus, $T^* \equiv (E/T.S.)(2/\sqrt{3})D_g$ (Eqn. 14)		
Sym	43.6	43.4
Asym	28.4	27.6
Extension rate, $D_{ext} \simeq (du/dl)_{min}$ (over 25 mm gauge length) (Eqn. 10)		
Sym	0.120	0.118
Asym	0.083	0.080
Profile growth displacement, u_g/l_0 (Fig. 6)		
Sym	0.278	0.280
Asym	0.138	0.133

rate is constant at $D_g = 0.09$, compared to the experimental value of 0.108. This tends to confirm the validity of (7) for finding the crack growth ductility from the slope of the load-displacement curve.

(g) Comparison with analysis

Equation (2) gives a crack growth ductility of 0.2, relatively independent of strain hardening. This is close to the crack growth ductility in the higher hardening alloys, but overestimates that in the lower hardening alloys by a factor of two. Notice, however, that this analysis is based on pure mode II deformation and a superposition of stationary singularities and does not take into account the hardening of the material left behind the growing crack. This indicates the need for a fully-plastic, incremental plasticity solution for a growing, mixed-mode crack in strain-hardening material, taking triaxiality into account.

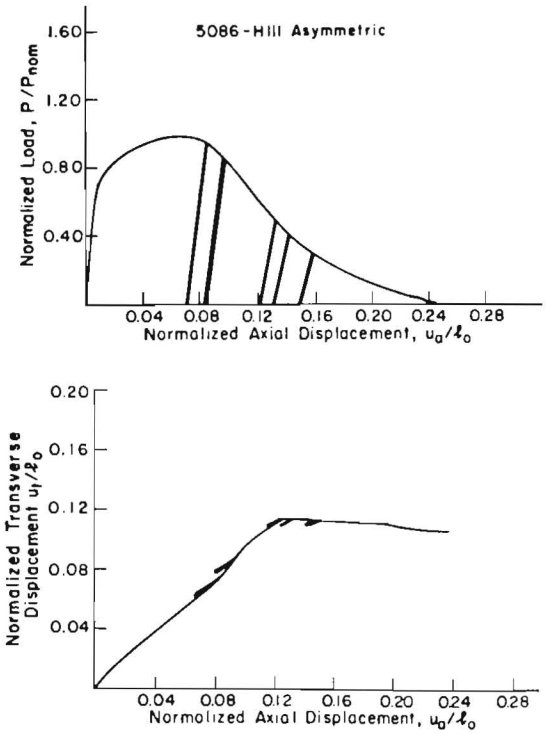

Fig. 11a. Test data for the 38.1 mm diameter 5086-H111 asymmetric specimens showing the unloading–loading points for making the crack front.

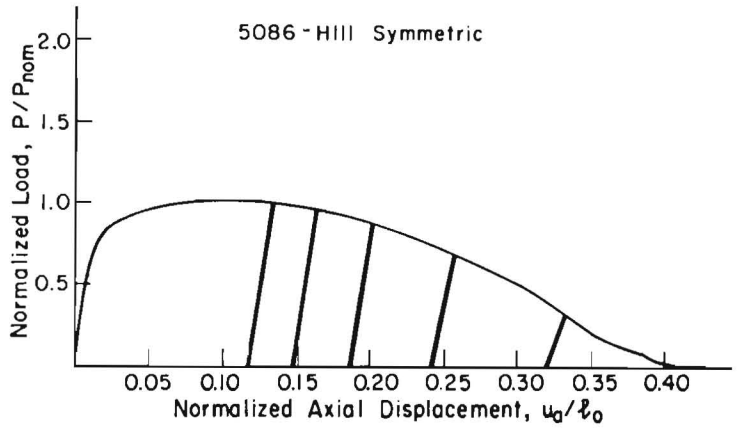

Fig. 11b. Test data for the 38.1 mm diameter 5086-H111 symmetric specimens showing the unloading–loading points for marking the crack front.

An accurate prediction of the crack growth orientation should account for spreading out of the deformation. In this context finite elements studies of the asymmetric specimens [26] predicted a crack orientation within two degrees of that observed experimentally, and a crack growth ductility for $n = 0.24$ twice that of $n = 0.12$.

The greater ductility of the symmetric, higher hardening specimens is also shown qualitatively by the higher ratio of sliding off to hole growth observed in electron fractographs [27].

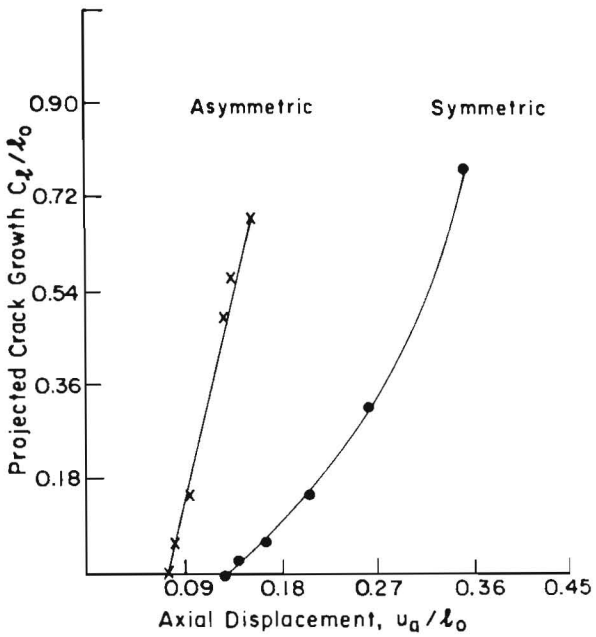

Fig. 12. Crack advance-axial displacement data for the specimens of Figs. 11a, 11b. The fatigue marks provided the crack positions.

4. Discussion

The previously defined crack growth ductility $D_g = du_c^p/dl$, the gauge displacement per unit reduction in ligament $D_{ext} = du/dl$, and the modified tearing modulus T^* are all measures of growth resistance for the fracture geometry of fully plastic asymmetric cracks. They are analogous to the crack opening displacement per unit crack advance, d(COD)/da, and the tearing modulus, T, or dJ/da by (11), (14), that have been defined and used for representing the propagation of ductile symmetric cracks. The values of D_g and D_{ext} for the symmetric specimens are comparable to those of d(COD)/da reported in the literature (see Table 1) for some common tests. In the asymmetric case, however, the low hardening alloys reduced these ductility measures by a factor of two to three. The central point is that single-parameter measures of ductile crack propagation are incomplete. Indeed, in this study the asymmetric geometry, incurring a change in the local distribution of strain, influenced the crack growth resistance. These ductility measures also depend on triaxiality because triaxiality as well as local strain distribution affects strongly the cleavage and hole growth mechanisms of crack growth.

Since the crack growth ductility must be greater than the compliance of the surroundings for stable fracture, stability is affected by both triaxiality and geometry. Loss of stability due to constraint has been discussed by Rice [28]. Paris et al. [6] developed instability relations for fully plastic (nonhardening) conditions, including some common configurations. For example, in the double edge-cracked strip in tension the imposed constraint leads to a critical value of T one sixth that in the center cracked strip in tension.

Summarizing our discussion, single-test characterization of crack propagation can apply only if crack extension occurs in a certain mode and configuration. Instead of a single parameter representation like d(COD)/da, *a set of such measures, each referring to a certain deformation mode and triaxiality*, is required to describe adequately the material resistance in crack propagation. In this study we have chosen to introduce D_g, not to emphasize a unique property, but because this definition pertains to the mixed mode fracture geometry and it is more closely related to structural needs. Extended work could involve testing asymmetric specimens under higher triaxiality, such as tensile testing on doubly grooved specimens with the asymmetry introduced through varying notch angles and positions; wedge-splitting of a doubly grooved specimen; or ductile fracture under asymmetric bending with the asymmetry introduced not only by specimen geometry but also through shear loading.

5. Conclusions

1. In asymmetric fully plastic configurations with only a single shear band (which can occur with cracks near welds for example), the crack progresses into prestrained material instead of the new material between the two shear bands of the symmetric case.
2. Specimens and a procedure to test the resulting effects on ductility have been developed and shown to be valid by a number of independent checks.
3. Experiments on six structural alloys have shown that the resulting reduction in crack growth ductility for high strength, low-hardening ($n \simeq 0.1$) alloys is a factor of about 3. In the higher hardening alloys ($n \simeq 0.2$) the reduction is no more than 20 percent.
4. The high crack growth rate of the asymmetric configuration leads to correspondingly higher stiffness requirements for fracture-stable design.
5. The initiation displacement for symmetric and asymmetric configurations is not much different, and was large compared to the displacement during growth. This ductility cannot always be counted on, however, for example in cracks growing by low cycle fatigue. Therefore the crack growth ductility should be measured and used in the design and maintenance of ductile structures.

In addition to the above major conclusions, there are several detailed ones.

6. The crack growth direction is 38–41 deg from the transverse (instead of 45 deg), as qualitatively expected from triaxial effects. The larger angle is with less strain hardening.
7. The average displacement vector is at about 51–63 deg from the transverse. Angles greater than 45 deg suggest a mode I deformation component.
8. Trebling the specimen size in 5086-H111 aluminum gave negligible size effect on the displacement to crack initiation, as expected, and appeared to reduce the crack growth ductility only by 4 percent.

Acknowledgements

The financial support of the Office of Naval Research, Contract N0014-82K-0025, and the interest and encouragement of the Project Monitor, Dr Y. Rajapakse, are both gratefully

acknowledged. The donation of the HY-80 and HY-100 steels by A. Wiggs of DTNSRDC is much appreciated. Also C. Beer and L.P. Pate were very helpful in editing and re-editing the manuscript.

References

1. H.W. Hayden and S. Floreen, *Acta Metallurgica* 17 (1969) 213–224.
2. C.D. Beachem and D.A. Meyn, in *Fractography*, ASTM STP 436 (1968) 59–88.
3. C.F. Shih, H.G. deLorenzi and W.R. Andrews, in *Elastic-Plastic Fracture*, ASTM STP 668 (1979) 65–120.
4. M.G. Dawes, in *Elastic-Plastic Fracture*, ASTM STP 668 (1979) 307–333.
5. C.G. Chipperfield, J.F. Knott and R.F. Smith, *Third International Congress on Fracture*, Munich (April 1973) paper I-233.
6. P.C. Paris, H. Tada, H. Ernst, and A. Zahoor, in *Elastic-Plastic Fracture*, ASTM STP 668 (1979) 5–36.
7. J.W. Hutchinson, *Journal of the Mechanics and Physics of Solids* 16 (1968) 13–31. See also ibid, 337–347.
8. J.R. Rice and G.F. Rosengren, *Journal of the Mechanics and Physics of Solids* 16 (1968) 1–12.
9. R.M. McMeeking and D.M. Parks, in *Elastic-Plastic Fracture*, ASTM STP 668 (1979) 175–194.
10. L.I. Slepyan, *Mekhanika Tverdogo Tela* 9 (1974) 57–67.
11. L.I. Slepyan, *Mekhanika Tverdogo Tela* 8, (1973) 139–148.
12. J.R. Rice, in *Mechanics of Solids*, Hill Anniversary Volume, H.G. Hopkins and M.J. Sewell (eds.), Pergamon Press, Oxford (1982) 539–562.
13. P. Ponte-Castañeda, Asymptotic Fields in Steady Crack Growth with Linear Strain-Hardening, Report MECH-69, Division of Applied Sciences, Harvard University, Cambridge, Massachusetts (1985).
14. P. Ponte-Castañeda, Report MECH-70, Division of Applied Sciences, Harvard University, Cambridge, Massachusetts (1985).
15. W.R. Andrews and C.F. Shih, in *Elastic-Plastic Fracture*, ASTM STP 668 (1979) 426–450.
16. F.A. McClintock, in *Fracture*, Vol. 3, H. Liebowitz (ed.), Academic Press, New York (1971) 47–225.
17. F.A. McClintock, *Welding Journal Research Supplement* 26 (1961) 202–208.
18. D.L. Jones and D.B. Chisholm, in *Fractography – Microscopic Cracking Processes*, ASTM STP 600 (1976) 235–248.
19. M. Chant, G. Green, I.J. Whatmough and D.C. Williams, The First Large Shear Specimen Test, General Electric Generating Board Report No. SSW/SSD/0250/R/83, Job No. 01–95 (1983).
20. C.F. Shih, in *Fracture Analysis*, ASTM STP 560 (1974) 187–210.
21. F.A. McClintock and A.H. Slocum, *International Journal of Fracture* 27 (1985) 49–62.
22. G.A. Kardomateas, F.A. McClintock and W.T. Cater, *Engineering Fracture Mechanics* 21 (1985) 341–351.
23. F.A. McClintock and A.S. Argon, *Mechanical Behavior of Materials*, Addison-Wesley, Reading, Massachusetts (1966).
24. F.A. McClintock, in *Physics of Strength and Plasticity*, A.S. Argon (ed.), MIT Press, Cambridge Massachusetts (1969) 307–326.
25. J.R. Rice and M.A. Johnson, in *Inelastic Behavior of Solids*, M.F. Kanninen (ed.), McGraw-Hill, New York (1970) 641–672.
26. G.A. Kardomateas, Mixed Mode I and II Fully Plastic Crack Growth from Simulated Weld Defects, Ph.D. thesis, Department of Mechanical Engineering, Massachusetts Institute of Technology, Cambridge, Massachusetts (1985).
27. G.A. Kardomateas, *Scripta Metallurgica* 20 (1986) 609–614.
28. J.R. Rice, in *Mechanics and Mechanisms of Crack Growth*, M.J. May (ed.), British Steel Corporation, Physical Metallurgy Centre Publication, Sheffield (1973) 14–39.

Résumé. La plupart des essais de rupture recourent à des éprouvette symétriques, où la fissure progresse dans une région relativement peu endommagée comprise entre deux zones déformées plastiquement par cisaillement. Cependant, une fissure au voisinage d'une soudure ou d'un épaulement, sollicitée dans le domaine plastique, peut ne comporter qu'une bande de glissement par cisaillement, le long de laquelle elle progresse, dans un matériau écroui et endommagé et comportant de ce fait une ductilité moindre que le matériau présent dans les configurations classiques.

Des essais sur six alliages ont montré que la ductilité par rapport à la croissance de la fissure, définie comme le déplacement minimum pour une réduction unitaire du ligament, est réduite d'un facteur 3 pour les alliages peu sensibles à l'écrouissage ($n = 0.1$) dans le cas assymétrique par rapport au cas symétrique. Cela signifie que des alliages à faible durcissement par écrouissage, par exemple les alliages à haute résistance, doivent présenter une structure environnante trois fois plus raide pour permettre une conception selon fissuration stable. Pour les alliages à sensibilité plus grande à l'écrouissage ($n \simeq 0.23$), la ductilité vis-à-vis de l'amorçage d'une fissure – à savoir ici le déplacement à la pointe de la fissure – est relativement peu affectée par l'asymétrie; cependant on ne peut pas toujours s'y fier pour exprimer la ductilité (p.ex. en fatigue olygocyclique). Dès lors, de tels essais de ductilité à la croissance d'une fissure sont utiles pour la conception et la surveillance des constructions.

Du fait de la triaxialité agissant sur un côté d'une fissure de cisaillement asymétrique, l'angle de cisaillement par rapport à la direction transversale se réduit de 45° à 38–41°, la plus petite divergence correspondant au plus faible écrouissage. En outre, le vecteur de déplacement du champ éloigné est incliné de 51° à 60° sur la direction transversale, d'autant plusque l'écrouissage est élevé, ce qui suggère qu'une composante de mode I prend place, même lorsque le champ de bandes de glissement sans durcissement laisse prévoir un cisaillement pur.